Numerical assessment of RANS turbulence models for the development of data driven Reduced Order Models

M. Salman Siddiqui[a,*], Adil Rasheed[b], Trond Kvamsdal[a,b]

[a] *Department of Mathematical Sciences, Norwegian University of Science and Technology, NO-7491 Trondheim, Norway.*
[b] *CSE Group, Mathematics and Cybernetics, Sintef Digital, 7034, Trondheim, Norway.*

Abstract

The ability to accurately predict vortex shedding around wind turbine blades is paramount, particularly at high Reynolds number. Turbulence models employed in the numerical studies strongly influence flow separation and the aerodynamic loading, thus affecting the overall accuracy of numerical simulations. In this manuscript, three turbulence models (Spalart-Allmaras, $k-\epsilon$ and $k-\omega$ Shear Stress Transport model) are investigated in two and three dimensional configurations using standard Reynolds Average Navier-Strokes equations. The focus is on the NACA0015 airfoil, and the simulations are conducted at a Reynolds number of 1.96×10^6 to match the experimental data in the literature. The effect of flow separation and vortex shedding pattern is investigated at different angles of attack ($0^\circ \leq \alpha \leq 17^\circ$,) along with the prediction ability of the turbulence models. Spectral analysis is performed over the time history of aerodynamic coefficients to identify the dominant frequencies along with their even and odd harmonics. A reduced-order model based on the van der Pol equation is proposed for the aerodynamic lift calculation. The method of multiple scales (a perturbation approach) is adapted to compute the coefficients of the proposed model consisting of quadratic and cubic non-linearities at the various angle of attacks (α). The model is also tested in a predictive setting, and the results are compared against the full order model solution.

Keywords: NACA0015 airfoil, Finite Volume Method, Reduce Order Models

1. Introduction

To determine a rapid and reliable estimation of the aerodynamic loading on the wind turbine structure, highly efficient tools are required [1–3]. Traditional designs have extensively relied on the analytical methods to study the parametric dependence of the geometrical parameters on loads of the structure [4, 5]. In this regard, initial estimations were based on Blade Element Momentum (BEM) theory [6] because of their computational efficiency. Researchers have also developed numerous tools based on simpler analytical methods (XFOIL [7] etc.) More sophisticated designs have utilized Computational Fluid Dynamics (CFD) methods [8–12]. Although the approach gives a better insight into the flow characteristics associated with the flow around wind turbine components, due to their exceptionally high computational cost it hasn't been utilized by designers to perform the parametric studies [3, 8], recently, researchers have started developing computationally efficient models employing Reduced Order Modeling (ROM) based on Proper Orthogonal Decomposition (POD) [13–16], Greedy Methods [17], a combination of Advanced Deep Neural Network [18–20] and turbulence modeling [21] coupled with traditional Navier Stokes Solvers [22] which are seen as major steps towards developing numerical models/approaches for parametric design.

Among various methods for the development of ROM, Phenomenological [23] based ROM employ Ordinary-Differential Equation (ODE) to model the parameters in a physical system. Self excited oscillators are an important examples in this category [24–26]. Such ROMs require

*Corresponding author
Email addresses: muhammad.siddiqui@math.ntnu.no (M. Salman Siddiqui), adil.rasheed@sintef.no (Adil Rasheed), trond.kvamsdal@ntnu.no (Trond Kvamsdal)

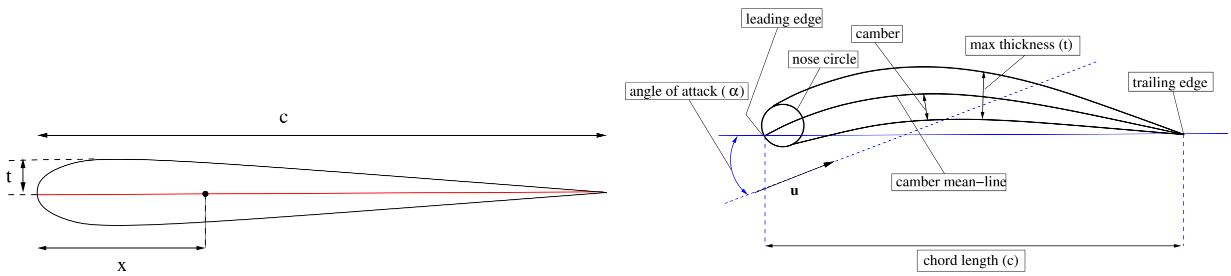

Figure 1: NACA0015: The left picture (a) shows a sketch of the standard symmetric airfoil designed by NACA, illustrating the base parameter required for its classification; such as chord length (c), thickness (t) and distance of the centroid from the leading edge (x). The picture on the right side (b) explain the different terminologies frequently employed in the design of airfoils.

accurate input data sets either from CFD simulations or experiments. These were previously developed in the study [27], where the time history of the aerodynamic coefficients was modeled using the self-excited oscillators. The nonlinear application of such ROM was identified in the study [28], where forced van der Pol oscillator was employed to model lift around circular cylinders at low Reynolds number (Re). The steady-state and transient modeling for lift and drag using van der Pol-Duffing models was found in the study [29], where the model has been manifested for accurate prediction ability of non-linear phenomenon on bluff bodies. The modeling of vortex-induced vibrations on the cylindrical riser for offshore applications is performed in [30] and the van der Pol based ROM models are developed for the prediction of lift and drag.

In the context of airfoil design, the CFD methods were previously employed in the study [31], to identify the turbulent flow structures around the blades. More recent work on such computations based on Isogeometric Finite Element methods [32] with SA and Variational MultiScale (VMS) turbulence models can be found in [33, 34]. Likewise several experiments [35–37] were conducted to quantify the performance of airfoils under different flow conditions. All the experiments were conducted in the wind tunnels, and the aerodynamic coefficients (C_l, C_d, C_p) were monitored. The main idea of the tests was to identify the stall on airfoils and determine the region in which sudden drop in the lift is experienced with an increase in the angle of attack, causing the flow to separate. Thus the studies focused on the unsteady boundary layer separation at higher Re over the airfoil surface and demonstrated the vortex shedding spectrum in the wake both in 2D and 3D spatial dimensions.

To standardize the numerical modeling for airfoils, the present manuscript is aimed towards examining the extent of turbulence models at higher Re of 10^6. The tests are conducted on the NACA0015 airfoil (owing to its availability of extensive experimental data), and simplified ROM models are proposed. The numerical setup is benchmarked against the published data available in the studies [37–39] in 2D/3D spatial dimensions for $k-\epsilon$, $k-\omega$ Shear Stress Transport(SST), Spalart-Allmaras (SA) models. The resolution of the flow field inside the transient boundary layer is analyzed, and the strength of the turbulence model is tested on the ability to capture the separation point ($\alpha_{critical}$). Spectral analysis is performed on the time history of aerodynamic coefficients to identify dominant frequency components. Perturbations methods such as the method of multiple scales are adapted, and coefficients of the proposed ROM model (based on van der Pol equation) are computed. In the end, the models are tested in a predictive setting, and their ability as a stand-alone forecasting tool is highlighted.

2. Theory

2.1. Symmetric 4-digit NACA airfoils

Standard 4-digit NACA airfoil is employed for the study [12]. The four numbers have a standard terminology, as defined by the National Advisory Committee for Aeronautics (NACA) for airfoils. The first, second and third-fourth numerals illustrate the maximum camber, the distance of maximum camber from the leading edge, and the most significant thickness, respectively. All the quantities are represented as a percentage of the chord length. Figure 1(b) exhibits relevant design parameters of the NACA airfoil.

The first two zero numerals represent the symmetric airfoils as illustrated in Figure 1(a). The schematics of the symmetric airfoils can be generated using the following formula

$$y_t = 5tc\left[0.2969\sqrt{\frac{x}{c}} - 0.1260\left(\frac{x}{c}\right) - 0.3516\left(\frac{x}{c}\right)^2 + 0.2843\left(\frac{x}{c}\right)^3\right] - \left[0.1015\left(\frac{x}{c}\right)^4\right] \tag{1}$$

here y_t, t, c, and x exhibits the width of airfoil thickness measured from the center, largest thickness, chord length and the distance between the leading to trailing edge respectively However, the Equation 1 does not provide a close curve at the trailing edge of the airfoil. Hence the equation is modified to get a closed geometry given by

$$y_t = 5tc\left[0.2969\sqrt{\frac{x}{c}} - 0.1260\left(\frac{x}{c}\right) - 0.3516\left(\frac{x}{c}\right)^2 + 0.2843\left(\frac{x}{c}\right)^3\right] - \left[0.1036\left(\frac{x}{c}\right)^4\right] \tag{2}$$

The Equation 2 has been used to develop the CAD model of the NACA0015 airfoil profile in the simulations of the present manuscript.

2.2. Turbulence modeling

To model the flow over NACA airfoil characterized by eddies with large spatiotemporal variations, RANS methodology is employed. Averaging the Navier-Stokes equations have introduced additional non-linear stress terms ($\rho\overline{v_i^{'}v_i^{'}}$) [40] which are related to the mean flow by the use of Boussinesq approximation. It has produced a constant term ν_t(eddy viscosity) [10] to describe the small-scale turbulent stress. Each turbulence modeled have solved additional equations to model the eddy viscosity. The detail of each model is outlined in the following subsection with the governing equations.

2.3. Governing equations

The fluid flow can be mathematically described by time-average mass (Equation 3) and momentum conservation equations (Equation 4).

$$\nabla \cdot (\rho \boldsymbol{u}) = 0 \tag{3}$$

$$\frac{D\boldsymbol{u}}{Dt} = -\nabla\left(\frac{p}{\rho}\right) + \frac{1}{\rho}\nabla \cdot \boldsymbol{R} + \mathbf{f} \tag{4}$$

here, $\boldsymbol{u}$ is a velocity vector, p is the pressure and ρ is the air density. $R_{ij} = \nu_t\left(\frac{\partial u_i}{\partial x_j} + \frac{\partial u_j}{\partial x_i}\right) - \frac{2}{3}k\delta_{ij}$ is the turbulent stress term that arise due to the time averaging procedure [41] and $\mathbf{f}$ represents the source terms.

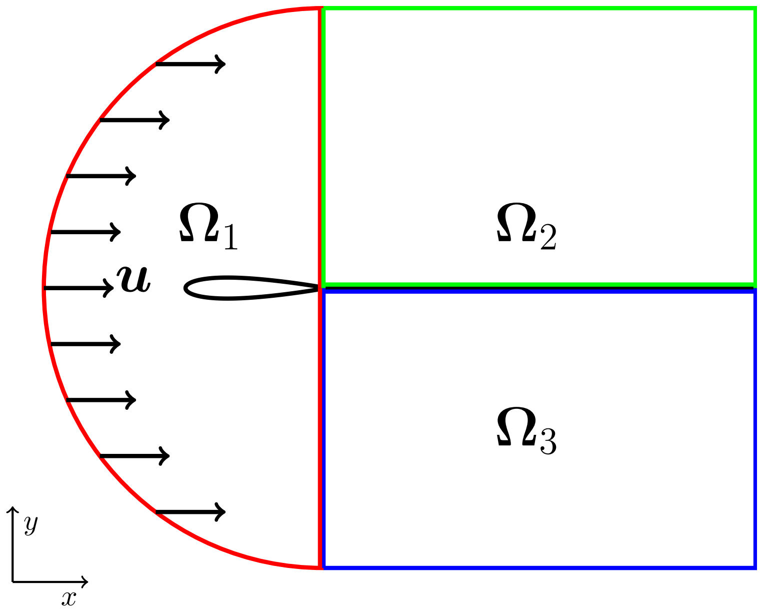

Figure 2: NACA0015: Schematic of the domain setup illustrating the domain patches for smooth generation of computational mesh around the airfoil.

2.3.1. Spalart-Allmaras (SA) turbulence model

The SA model solve one additional transport equation to compute the eddy turbulent viscosity. It was initially designed for external flow problems related to aviation and aerospace industry [42]. Due to similar Reynolds number regime (10^6) in mega watt size wind turbines applications, it is expected to produce good results. The governing equations of eddy viscosity is described in Equation 5. For detailed explanation of the model and the constants terms employed in the design as originally established by Spalart, the reader is referred to [42], see also [33] and references therein for recent advances

$$\frac{\partial \tilde{\nu}}{\partial t} + \boldsymbol{u} \cdot \nabla \tilde{\nu} = Q(\tilde{\nu}) + \frac{c_{b2}}{c_{b3}} \nabla \tilde{\nu} \cdot \nabla \tilde{\nu} + \frac{1}{c_{b3}} \nabla . [(\nu + \tilde{\nu}) \nabla \tilde{\nu}] \tag{5}$$

where, ν is the fluid viscosity, $\tilde{\nu}$ is the viscosity like variable used to model turbulence. $Q(\tilde{\nu})$, c_{b1}, c_{b2}, c_{b3} are model constants.

2.3.2. $k - \epsilon$ turbulence model

The turbulent eddy viscosity is modeled by equations of turbulent kinetic energy (k) and turbulent dissipation (ϵ). These two equations associate the mean flow quantities to internal turbulent stresses (Equations 6-7). In the literature, this model has been found to perform well away from the wall in the free shear regions. Because of its in-discrepancy to model the viscous sublayer accurately, wall functions are used to avoid the concentration of mesh near the surface (to allow first cell node to be placed in the log-law region). The Equation 6 for turbulence kinetic energy (k) and Equation 7 for turbulent dissipation is employed. For further explanation of the model, the reader is encouraged to read [43]

$$\frac{\partial k}{\partial t} + \boldsymbol{u} \cdot \nabla k = \nabla \left[\frac{\nu + \nu_t}{\sigma_k} \nabla k \right] - \epsilon + \tau_{ij} \nabla \boldsymbol{u} \tag{6}$$

$$\frac{\partial \epsilon}{\partial t} + \boldsymbol{u} \cdot \nabla \epsilon = \nabla \left[\frac{\nu + \nu_t}{\sigma_\epsilon} \nabla \epsilon \right] + C_{\epsilon 1} \frac{\epsilon}{k} \tau_{ij} \boldsymbol{u} - C_{\epsilon 2} \frac{\epsilon^2}{k} \tag{7}$$

where, ν is the fluid viscosity, ν_t is the turbulent viscosity. τ_{ij} is the tensor representing the turbulence stress ($\overline{\boldsymbol{u}_i' \boldsymbol{u}_j'}$), $C_{\epsilon 1}$ and $C_{\epsilon 2}$ are model constants. $y^+ = \frac{u_\star y}{\nu}$, the non-dimensional wall

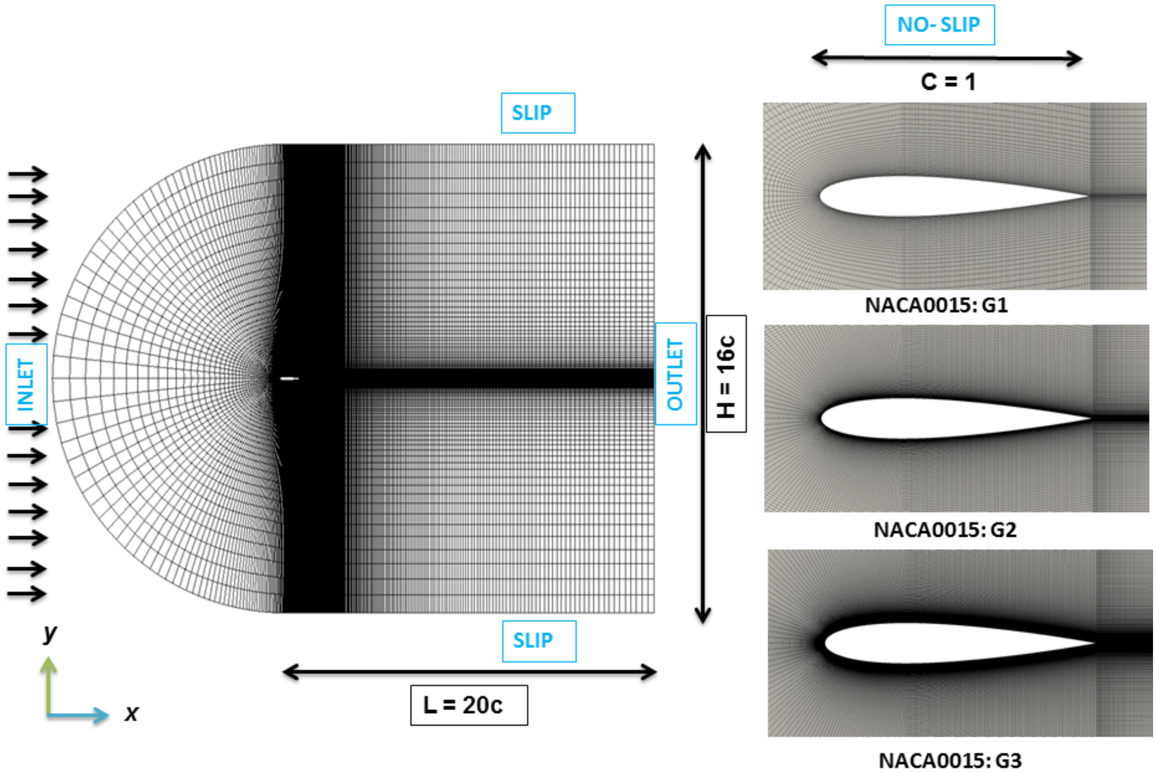

Figure 3: NACA0015: Description of boundary conditions and structured computational grid utilized to perform the high fidelity simulations together with the overall dimensions of the computational domain, as a function of the airfoil's chord length (c = 1). The column on right-hand side represents different mesh gradings employed to identify the grid independence. ($\mathbb{G}_1$ = 52450, $\mathbb{G}_2$ = 75840, $\mathbb{G}_3$=120650)

distance (where $u_\star$ is the friction velocity at the nearest wall, y is the distance to the nearest wall and ν is the local kinematic viscosity of the fluid), has been maintained in the log-law region between $30 \leq y^+ \leq 100$ such that the wall functions calculate the correct values of the field variables for the neighboring cells adjacent to the wall. To avoid generation of stagnation points, limiters introduced by Kato and Launder [44] are used, who consider that the stagnation points are irrotational, with minimal vorticity (Ω), thus the limiter terms becomes $G_k = \mu_t S Q$, where (Ω) is the magnitude of vorticity $\Omega = \sqrt{2\Omega_{ij}\Omega_{ij}}$.

2.3.3. $k-\omega$ SST turbulence model

To model eddy viscosity, it solves $k-\omega$ in the inner part of the boundary layer and transition to $k-\epsilon$ in the free stream region. The SST formulation regulates the transition between the models. Menter [45] introduced a blending function which controls the switching between ω and ϵ equations.

Turbulent kinetic energy and rate of dissipation of eddies are given by Equation 8 and 9. For a detailed explanation of the model and constant terms, the reader is referred to [45]

$$\frac{\partial k}{\partial t} + \boldsymbol{u} \cdot \nabla k = \nabla \left[\frac{\nu + \nu_t}{\sigma_k} \nabla k \right] - \omega k + \tau_{ij} \boldsymbol{u} \tag{8}$$

$$\frac{\partial \omega}{\partial t} + \boldsymbol{u} \cdot \nabla \omega = \nabla \left[\frac{\nu + \nu_t}{\sigma_\omega} \nabla \omega \right] + \frac{\mathit{\Gamma}}{\nu_t} \tau_{ij} \boldsymbol{u} - \omega^2 \beta + 2(1 - F_1) \frac{\sigma_{\omega 2}}{\omega} \nabla \omega \nabla k \tag{9}$$

τ_{ij} is the tensor representing the turbulence stress $(\overline{\boldsymbol{u}_i' \boldsymbol{u}_j'})$, F_1 is the blending function, $\mathit{\Gamma}$, σ_ω and $\sigma_{\omega 2}$ are the model constants. y^+ has been maintained in the buffer region for the simulation between $5 \leq y^+ \leq 30$ such that the wall functions sets the correct ω and k at the wall for each first cell. The excessive generation of the turbulence energy in the vicinity of stagnation points is

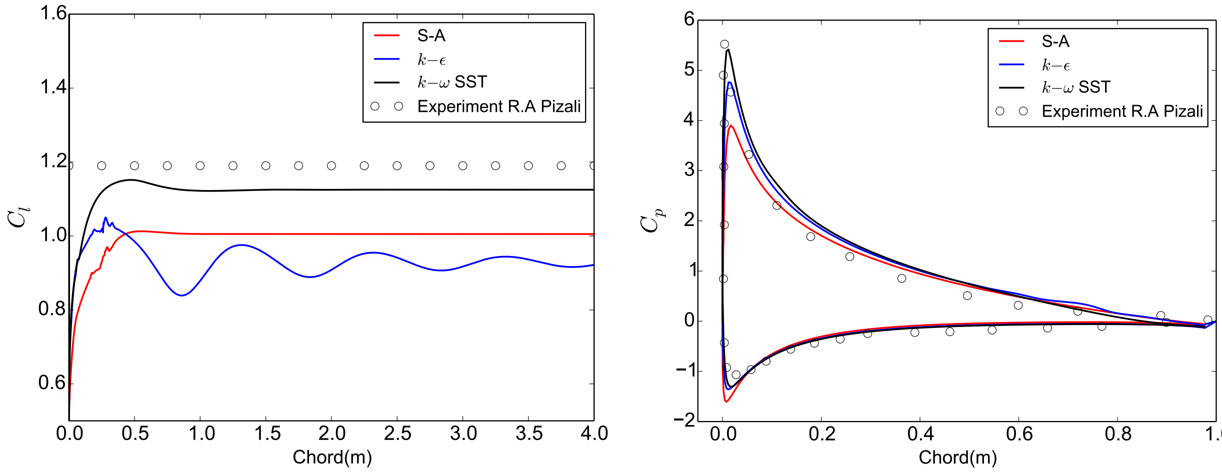

(a) Cumulative mean C_l (b) Cumulative mean C_p

Figure 4: NACA0015: The left picture (a) exhibits the time history of the lift coefficient for the three turbulence models at $\alpha = 13°$ showing convergence history. The right picture (b) reports the comparison of C_p values for the three different turbulence models with the experimental data of Pizali et al. [37] at Re=1.96x10^6.

controlled by using the limiters as introduced by mentor $G_k = min(G_k, C_{lim}\rho\omega)$, where the C_{lim} has a default value. The use of limiters avoids stagnation points to appear in the aerodynamic simulation without altering the shear layer performance.

2.4. Aerodynamic coefficients

The performance parameters are studied over a range of α at a particular Re. The Re is defined as [46]

$$Re = \frac{u_\infty c}{\nu}$$

here, u_∞ is the incoming velocity and $\nu = \mu/\rho$ is the kinematic viscosity. The aerodynamic coefficients of drag (C_d), lift (C_l) and pressure (C_p) are governed by following equations [47]

$$C_d = \frac{F_x}{\frac{1}{2}\rho u_\infty^2 cl}, \quad C_l = \frac{F_y}{\frac{1}{2}\rho u_\infty^2 cl}, \quad C_p = \frac{p - p_\infty}{\frac{1}{2}\rho u_\infty^2}.$$

3. Simulation setup

In this section, a full description of the simulation set up is provided regarding the choice of domain size, mesh resolution, selection of initial/boundary conditions, time step size, and solver settings.

3.1. Domain size and meshing strategy

A multiblock approach has been adapted to allow more control over the generation of computational mesh (see Figure 2). It has provided flexibility near the sharp corners, and also to conformed well to the underlying geometry. Equation 2 is employed to construct a smooth NACA 0015 profile. The computational domain is subjected to a body-fitted C-type mesh. Quality orthogonal cells are clustered due to the presence of sharp gradients arising from the rapid changes in the flow physics on the surface and the wake region of the airfoil. It also enabled a smooth transition from the airfoil surface towards the outer flow field with quality hexahedral elements. Three sets of mesh grading are generated ($\mathbb{G}_1, \mathbb{G}_2, \mathbb{G}_3$) to perform the mesh independence study. $\mathbb{G}_2$ grading factor has adequately captured the dynamics of flow and provided accurate values of aerodynamic coefficient value with the least computational time (see Figure 3). The extent of the computational domain is selected by a domain sensitivity study, details of which can be found in the previously published article by the authors [33]. Based on the study, a domain size of 20c in the downstream direction, 8c in the upwind direction and a circular arc of radius 8c connecting the upper and lower surface are employed. The 2D mesh is extruded with the same underlying mesh topology to obtain the 3D computational domain. Mesh information of both the spatial dimensions can be found in Table 1.

3.2. Time step

Selection of u_∞, grid(Δx) and time step size(Δt) is done such that the overall numerical stability of the solution remains intact. To keep track of stability, the Courant number ($C = \frac{u_\infty \Delta t}{\Delta x}$) is monitored and designed to remain less than one. OpenFOAM-4.0 (OF-4.0) has a unique feature of self-adjusting the time step size based on the Courant number constraints, which has been used to bound the solution. An initial accurate time step estimation is still required for maintaining the overall accuracy of the solution. Therefore, a time independence study has provided an accurate estimate of the initial time step. A time step size of 0.0001 seconds is observed to produce time-independent results for lift and drag coefficients. Thus it is selected as the initial time step size for the simulations in the manuscript.

3.3. Initial and boundary conditions

The simulation has been first validated against the experimental test of Pizali et al. [37]; therefore, the numerical framework and boundary conditions are selected to match consistently with the experimental setup of the authors. The flow constants are based on a reference fluid density $\rho = 1.225$ kg/m^3, dynamic viscosity of $\mu = 1.82 \times 10^{-5}$ kg/m.s, constant flow velocity of $u_\infty = 20$ m/s and the $Re = 1.96 \times 10^6$. The flow field is assumed fully turbulent, and the transition from laminar to turbulent regime inside the boundary layer is not explicitly modeled on the upper and lower surface of the airfoil. Velocity Inlet boundary condition is employed at the inlet with the fixed value of velocity $u_\infty(20, 0, 0)$. Outflow condition is imposed on the opposite side of the domain and assigned a constant value of zero pressure drop. Upper and lower walls are subjected to slip boundary conditions. The computational domain is extended to a unit length in the third dimension as OF-4.0 required a unit dimension in the normal direction for computing the solution. The two new boundaries in 2D; Front and Back are subjected to symmetry boundary conditions. No-slip condition is employed for the airfoil upper and lower surface with zero pressure gradients. Specialized wall functions in OpenFOAM have been used, i.e., epsilonWallFunction, omegaWallFunction, kqRWallFunction [48] are utilized to relax the concentration of mesh resolution near the airfoil surface. To provide an accurate estimate of the initial flow field, an analytical solver is run first, which has improved convergence and reduced the overall simulation time. The schematic of different boundary conditions imposed on the computational setup is shown in Figure 3.

Mesh Statistics				
Dimensions	Cell type	Cells	Faces	Nodes
2D	Hexahedral	75,840	304,113	153,186
3D	Hexahedral	2,275,200	6,924,030	2,374,383

Table 1: NACA0015: Details of the computational mesh used for the 2D and 3D numerical study. A structured mesh is generated for both spatial dimensions with quality hexahedral elements. The mesh topology between the two dimension is kept the same to eliminate the possible discrepancies in results due to uneven cell distributions in the two spatial dimensions.

3.4. Solver setting

The present solver within the OF-4.0 [49, 50] framework is utilized. To impose the continuity constraints, an elliptic equation of pressure is employed by imposing the divergence constraints on the momentum equation. This procedure forms a pressure modified equation which is solved in a segregated manner with the turbulence equations. A PIMPLE (combination of PISO-SIMPLE) algorithm is employed, which has allowed taking bigger steps in the temporal direction. The equations are discretized in a finite volume technique and integrated over Control Volumes (CV) using the Green-Gauss divergence theorem. Thus, volume integrals are transformed into surface integrals of the CV. Second order linear discretization is employed for all the equations (except k and turbulence equations which used upwind convection). The gradient term is divided by a sum coming from orthogonal and non-orthogonal parts. Full non-orthogonal correction is realized for all equations as solver stability is not trivial owing to the utilization of particular computational mesh. To solve the systems of governing equations, Geometric Agglomerated Algebraic Multigrid (GAMG) solver is employed. The solution time is reduced by applying DIC Gauss-seidel as a smoother, which damp the oscillations in the solution and enhances convergence [51]. The convection terms are discretized with bounded Gauss upwind since it is known to be less dissipative and highly stable [51]. For the solution of diffusion term in the NS equation, Gauss linear corrected is employed. The first order implicit scheme is used for the solution of time marching term. The magnitudes of density and pressure are by extrapolating the data from the centers of the neighboring points.

3.5. Simulation length

Convergence is achieved for the flow field variables using the time step size obtained from the independence study ($\Delta 0.0001$) seconds. Accurate estimation of the aerodynamic coefficients is obtained in connection with the experimental results. Simulations results for low α required approximately three thousand time iteration to reach convergence (see Figure 4(a)). However, simulations at higher α required approximately ten thousand time levels to meet the convergence criteria (Residuals $\leq 10^{-6}$). Cumulative lift and drag values are monitored in parallel to determine if the steady-state values are achieved.

3.6. Definition of test cases

First the numerical setup is validated at $\alpha = 0°$. Then multiple test cases are run for two-dimensional analysis. Simulations are performed over range of α i.e. $\alpha = 0°$, 2°, 4°, 5°, 7°, 9°, 11°, 13°, 15°, 17°, using all the three turbulence models. To conduct 3D simulations, 2D cases are extruded in the third direction with a fixed mesh topology. Sixty cases are numerically investigated in this entire study, and the performance parameters (C_l, C_d, C_p) are carefully monitored.

4. Results and discussion

The results are presented for each turbulence models over the range of α. By monitoring the flow behavior over the airfoil surface, three flow regimes are recognized. The first regime is identified as the *attached-flow* regime ($0° \leq \alpha \leq 11°$), inside which the streamlines remain attached to the airfoil's upper and lower surfaces. A mild separation starts to appear inside *secondary-flow* regime ($11° < \alpha \leq 13°$), and the flow streamlines begin to separate from the airfoils trailing edge. The detachment in the flow is not enough at this stage to cause oscillations to appear in the lift and drag values. In the *stall-flow* regime ($13° < \alpha \leq 17°$) the airfoil experiences a dramatic loss in the lift coefficient and vortex shedding starts to appear in the form of leading and trailing edge vortices. These intermittent rotational vortices get combined in the wake and generate a von Karman vortex street [52, 53]). A sudden rise is the magnitudes of drag coefficients are also observed at this point. Because of vortex shedding, the magnitudes of the aerodynamic coefficient keep oscillating about a mean value.

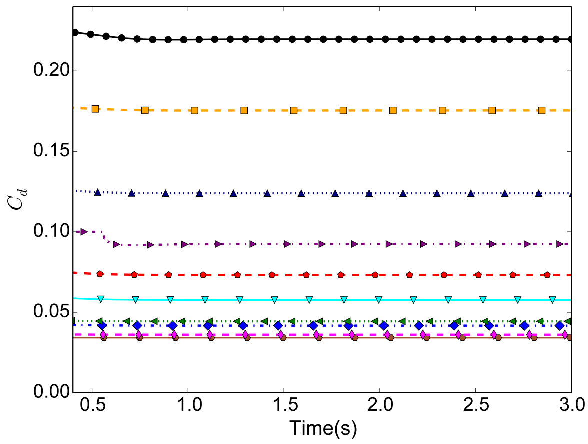

(a) Coefficient of drag; S-A turbulence model

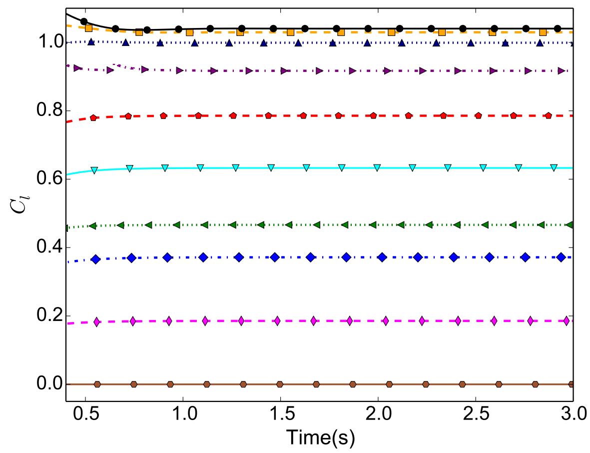

(b) Coefficient of lift; S-A turbulence model

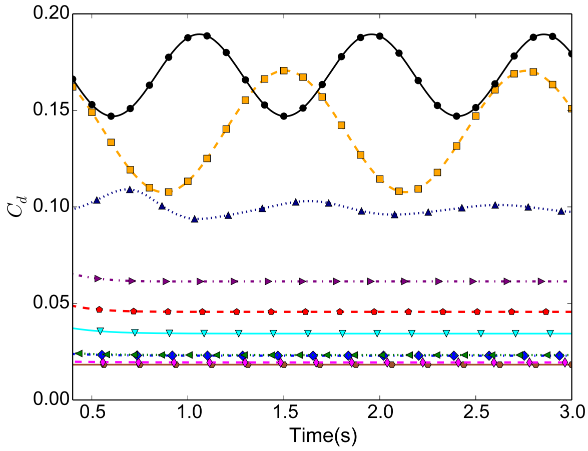

(c) Coefficient of drag; $k-\epsilon$ turbulence model

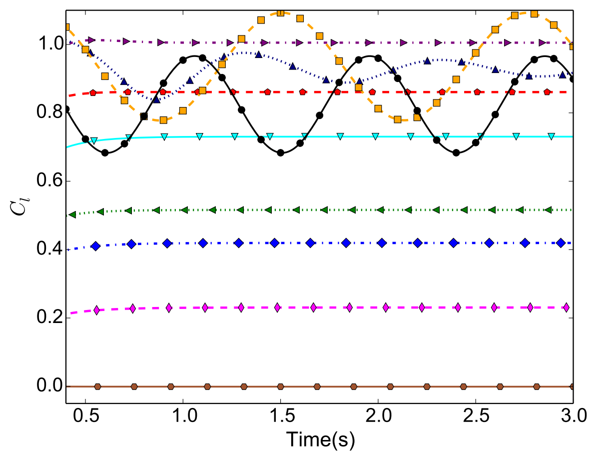

(d) Coefficient of lift; $k-\epsilon$ turbulence model

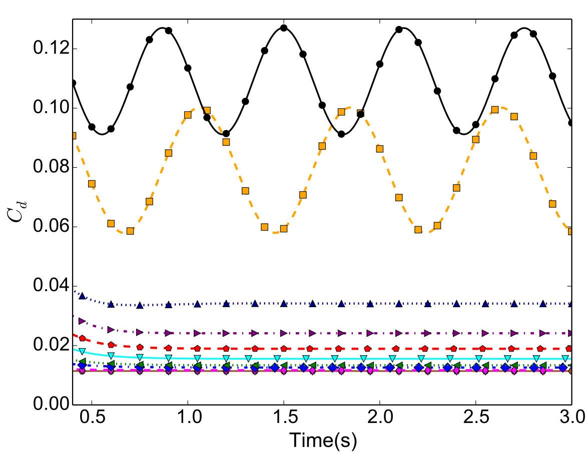

(e) Coefficient of drag; $k-\omega$ SST turbulence model

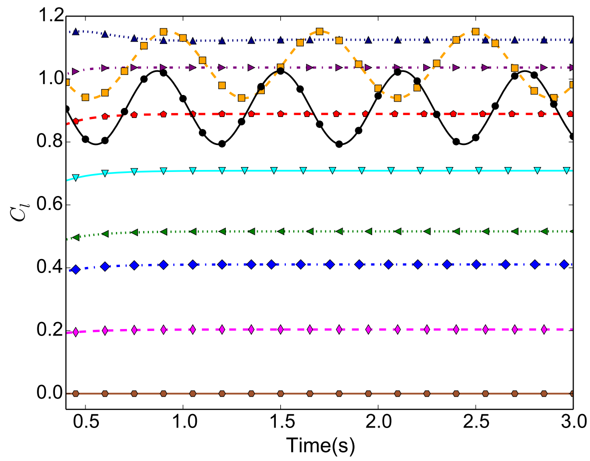

(f) Coefficient of lift; $k-\omega$ turbulence model

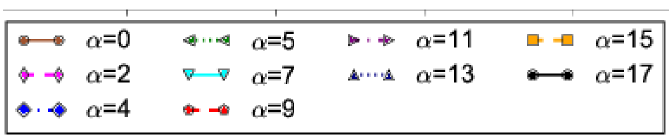

Figure 5: NACA0015: Temporal history of aerodynamic coefficients at $0° \leq \alpha \leq 17°$ for 2D

4.1. Time history and convergence

Rapid convergence rates are observed for the simulations conducted in the *attached-flow* regime. First few hundred time steps manifested initial instabilities in the coefficient values; however, all the solutions for the *attached-flow* achieved convergence within 1000 times step iterations. Among the models, faster convergence rates are observed for SA model, which is mainly due to the solution of only one additional transport equation for the prediction of small-scale turbulence. No oscillations in the aerodynamic coefficients are reported for $\alpha \leq 11°$ for any turbulence model, which is a manifestation of attached flow around over the airfoil. Oscillations started to appear for $k-\epsilon$ and $k-\omega$ SST inside mild separation regime. Even at this point, SA model predicted constant values of coefficients with no sign of vortex shedding. In terms of the convergence rates, $k-\omega$ SST have shown superior performance as compared to $k-\epsilon$, which have taken approximately $20,000$ iterations to reach the desired residuals $\leq 10^{-6}$. Vortex shedding of various size and strength is observed from the time history of aerodynamic coefficients for $k-\omega$ SST and $k-\epsilon$ turbulence models. $k-\omega$ SST models dominated the vortex frequency and strength as compared to the $k-\epsilon$. Figure 5 provides a quantitative comparison, further explanation using spectral analysis will be outlined in section 4.5.

4.2. Drag, lift and pressure coefficients

In general, $k-\omega$ SST and $k-\epsilon$ have shown a good comparison with the experimental data, unlike the SA model which failed altogether to capture the stagnation point and the flow separation. For the $k-\omega$ SST and $k-\epsilon$, smaller differences in the magnitudes of surface pressure distributions have produced substantial variations in the lift and drag values prediction by each model. The monitored values of the aerodynamic coefficients are presented in the subsequent section.

4.2.1. Lift (C_l)

The lift coefficients for the $k-\omega$ SST, $k-\epsilon$ and SA turbulence models are in good agreement with experiments at most incidence angles. In particular, $k-\omega$ SST model has shown the good estimates at all incidence angles. The SA model has performed well at lower α, but shows unsatisfactory behavior at α in the stall regime. The $k-\epsilon$ model have shown discrepancies to predict transition between flow regimes. However, $k-\epsilon$ are better than $k-\omega$ SST for $\alpha = 15°$ and $17°$.

4.2.2. Drag (C_d)

For the prediction of drag coefficient, only $k-\omega$ SST model have shown a good match against the experimental data. Whereas, the $k-\epsilon$ model has only shown reasonable estimate of drag coefficients inside the attached flow regime. For the mildly separated and stall regions, it has produced higher values. SA model, on the other hand, over-predicts the values throughout the band of numerical simulations under all regimes.

4.2.3. Pressure coefficient (C_p)

Comparison of the pressure coefficient at α=17° is shown in Figure 4. It can be observed that all models match consistently well with the C_p predicted by the experiments. SA model reports higher values of C_p at bottom surface of the airfoil, whereas on the top surface it exhibits lower value unlike the other models. A similar trend of C_p is observed on the top and bottom surface of the airfoil for $k-\epsilon$ and $k-\omega$ SST model. The magnitude of C_p at the lower surface is less for $k-\epsilon$ in comparison to the $k-\omega$ SST. In general, $k-\omega$ SST model compares well against the experimental data consistently. This manifests the ability of $k-\omega$ SST model to predict accurate pressure distribution around the airfoil surface, which is also paramount for the accurate prediction of lift and drag magnitudes. Similar results were also identified by Tachos et al. [54]

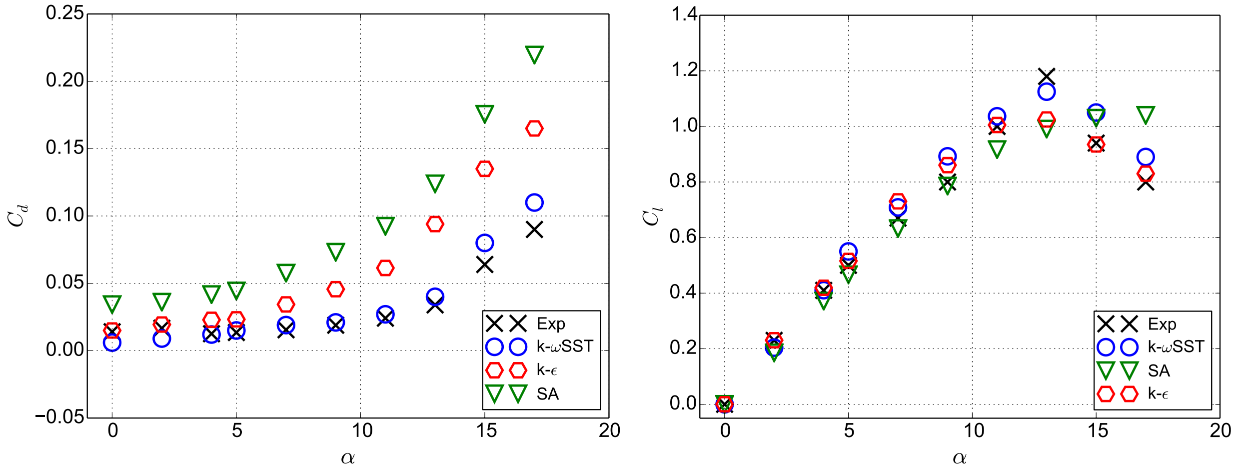

(a) Drag (b) Lift

Figure 6: NACA0015: The left picture (a) shows the comparison of cumulative drag prediction by each turbulence model over the range of α. A continuous rise in the prediction from the turbulence models is observed. The picture on the right side (b) shows the comparison of lift, where $k-\omega$ SST shows excellent comparison with the experimental values of Piziali et al. [37] over the range of α and Re=1.96x10^6.

4.3. Prediction of stall and flow structure characterization

The SA model is not able to capture the flow detachment point ($\alpha_{critical}$) for the airfoil (see Figure 6(a)). Even though it predicts the magnitude of lift coefficient in the vicinity of the experimental data, the overall trend for the lift profile is observed to increase with the rise of incidence angles. This is believed to happen since SA model adds only a single additional variable for an undamped kinematic eddy viscosity and is effective model at low-Reynolds number regime in its original form. It does not accurately compute fields that exhibit shear flow, separated flow, or decaying turbulence [55] at higher Reynolds number. For the present investigations, wall functions [48] are employed to improve its prediction capability towards the flow around NACA0015 airfoil. The $k-\epsilon$ and $k-\omega$ SST models accurately represent the flow separation point ($\alpha_{critical}$=13°) which is found to be in agreement with the behavior of the aerodynamic coefficients observed in the experiments. An increase in the angle of attack from 15° to 17° implies a sudden loss of lift and a dramatic rise in drag (see Figure 6(a)-6(b)). The obtained results from each model is summarized in Table 2 corresponding to the experimental data. To study the qualitative behavior, snapshots of velocity magnitude are plotted at α = 13°, 15°, 17° to highlight qualitative differences between the turbulence models. Each model has captured certain amount of separation along with vortex shedding of variable size and strength. The examination of contours in Figure 8 highlights the position of flow reversal point. The SA model produced the least amount of reverse flow at higher α. No oscillations are reported in the time history of aerodynamic coefficients for both C_l and C_d as observed in section 4.2.

	α=13°		α=17°	
Turbulence Model/Experiments	C_l	C_d	C_l	C_d
Experiment (Pizali et.al [37])	1.15	0.0331	0.807	0.091
k-ω SST model	1.125	0.034	0.911	0.110
k-ϵ model	1.025	0.094	0.832	0.165
SA model	0.990	0.129	1.052	0.219

Table 2: NACA0015: Quantitative comparison of lift and drag coefficients between the experimental data of Pizali et al. [37] and three turbulence models at α = 13° and α = 17°; Re = 1.96 x 10^6.

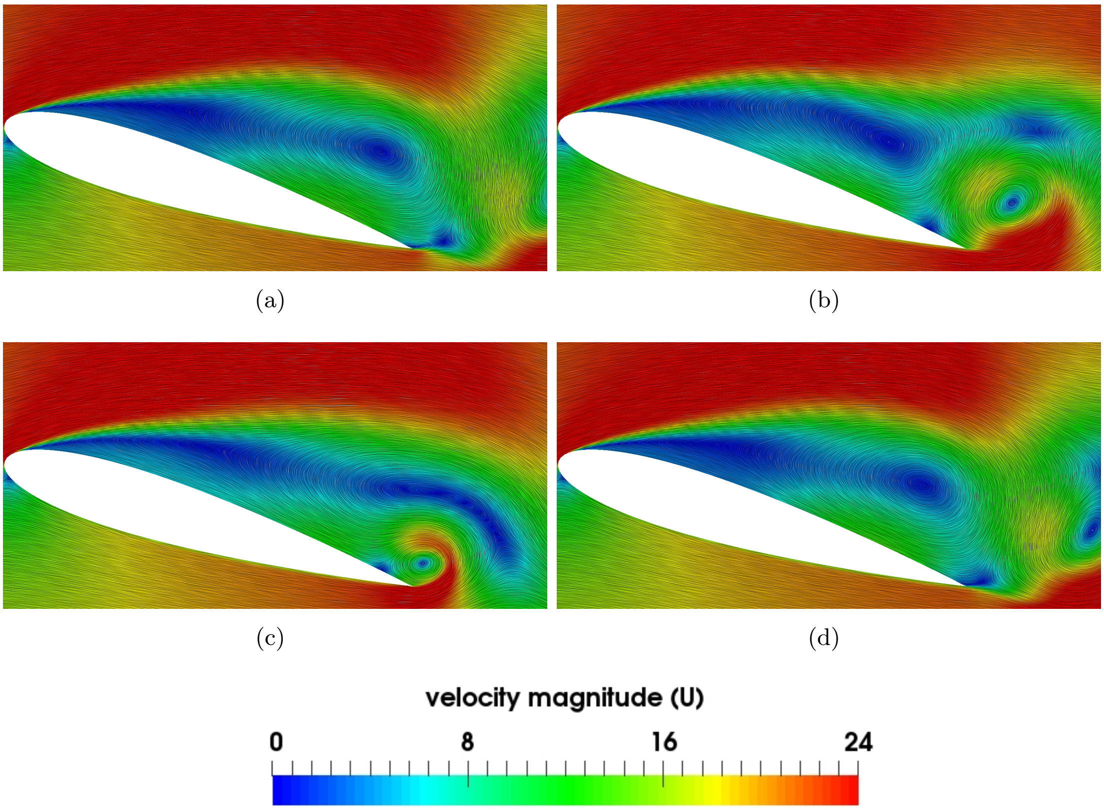

Figure 7: NACA0015: Contours of velocity field superimposed with streamlines representing the vortex roll up and detachment phenomenon from the airfoils upper surface. These vortices leaving the surface cause unstable pressure distribution and results into highly unstable flow in the wake. The snapshots are taken a four different time steps for $k-\omega$ SST turbulence model at α=17°; Re=1.96x10^6

Whereas the $k-\omega$ SST model gives the largest reverse flow behind the wake of airfoil. This unsteadiness in the flow is explicitly visible in Figure 6(a). A similar flow pattern is identified for $k-\omega$ SST and $k-\epsilon$ at α=15°. The flow characteristics of stall regime have shown sharp intermittent trailing and leading edge flow separation. This causes highly non-linear behavior, which is characterized by the shedding of circular eddies developed into a von Karman vortex street. To better understand the evolution of vortex shedding, snapshots of streamline over the airfoil are plotted in Figure 7. Development of flow reversal point portrays the evolution of stall vortex and phenomenon of flow separation. Initially, the flow starts to separate from the trailing-edge region, then move towards the leading edge until the flow reversal point is reached. Stall vortex thus first develops, peak in size before moving away from the surface. The point of flow reversal also moves away from the leading edge with the shedding of the vortex.

4.4. 2D versus 3D simulations

Baseline mesh of 2D is extended a unit dimension in the third direction (z) with underlying mesh parameters untouched. The boundary condition are switched from two-dimensions ($\frac{\partial}{\partial z}=0$) to three-dimensions ($\frac{\partial}{\partial z} \neq 0$) on the upper and lower surface of the domain, such that a three-dimensional solution can be calculated. The present numerical setup is motivated from the studies conducted in [56] which has adopted similar configuration to study the three-dimensional characteristics for asymmetrical S826 airfoil. A significant increase in the simulation time is experienced for 3D simulation in comparison to the 2D (approximately five times more). Vorticity along the spanwise direction is plotted in Figure 9(a) which depicts a consistent flow pattern throughout the blade length in the z-direction. No transverse flow distribution is observed, which is considered a prime reason for similar flow pattern in the third spatial dimension.

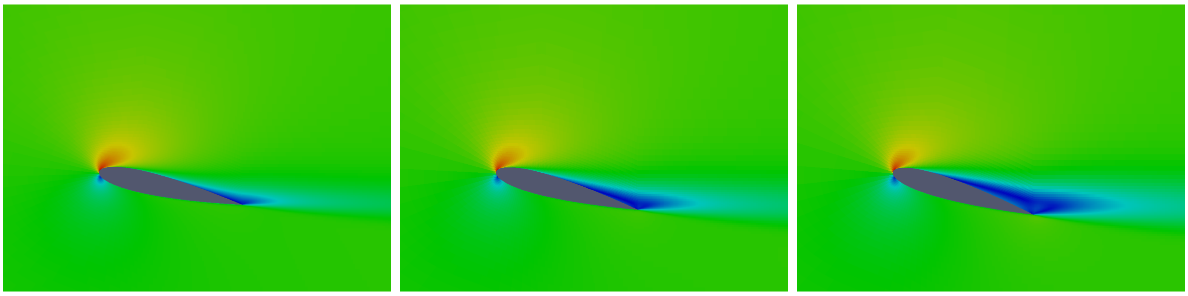

(a) α=13°, S-A model (b) α=15°, S-A model (c) α=17°, S-A model

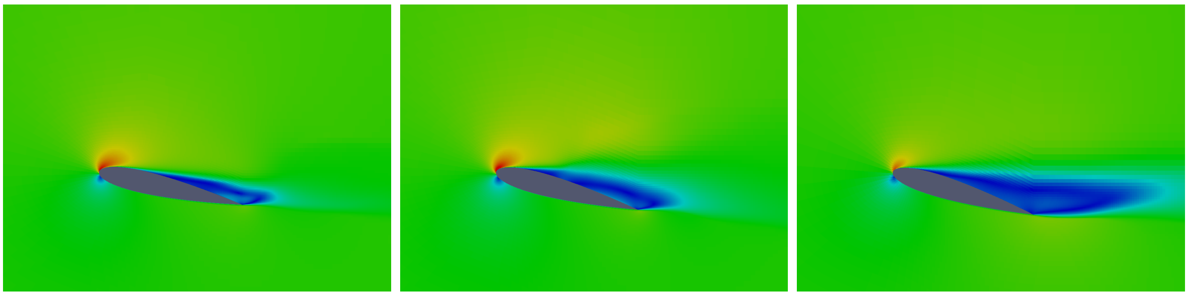

(d) α=13°, $k-\epsilon$ model (e) α=15°, $k-\epsilon$ model (f) α=17°, $k-\epsilon$ model

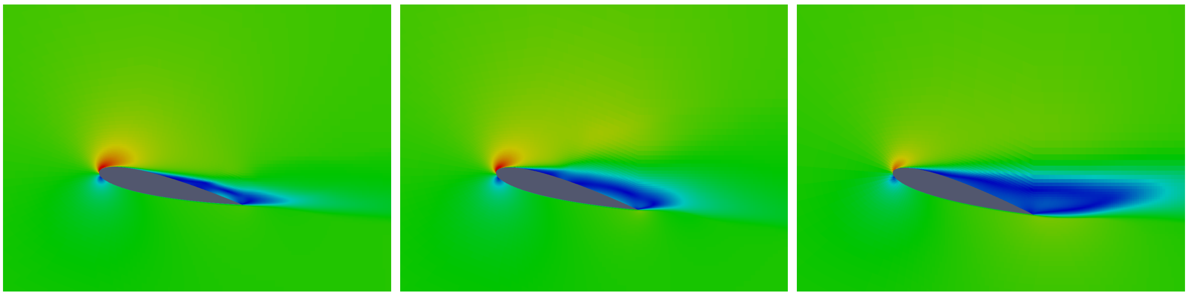

(g) α=13°, $k-\omega$ model SST (h) α=15°, $k-\omega$ SST model (i) α=17°, $k-\omega$ SST model

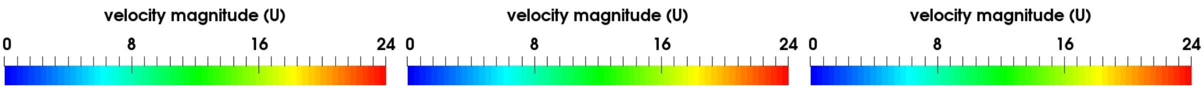

Figure 8: NACA0015: Contours of velocity magnitude illustrating the comparison of three turbulence models at α in stall regime and Re=1.96x10^6. It is evident that the SA-model gives consistently smaller flow separation than the other two models. $k-\omega$ SST and $k-\epsilon$ results in comparable magnitudes of the vortex shedding.

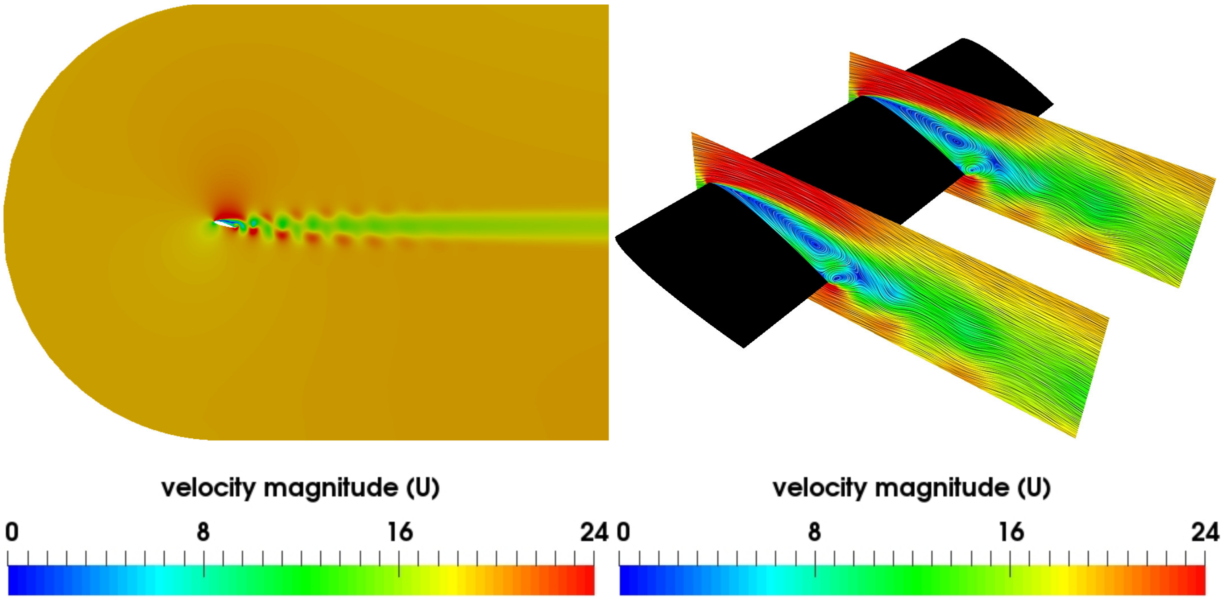

Figure 9: NACA0015: The left picture (a) exhibits the formation of coherent structure formation in spatial two dimensions. Von Karman vortex street is clearly visible in the wake of the airfoil. Similar behaviour was previous identified by Nayfeh et al. [27]. The picture on the right side (b) illustrates the coherent structure formations on two planes located at two distances (0.3 and 0.8) in the z-direction. The velocity contours superimposed with streamlines suggests lack of 3D effects due to similar flow profile. The contours are plotted for $k-\omega$ SST at α=17°; Re=1.96x10^6.

The contours of flow spectrum superimposed with the streamlines positioned at 0.3z and 0.8z are illustrated in Figure 10. Vortex stretching is visible in the wake structure behind the airfoil in both dimensions. The extent of flow separation distinctly indicates the stall regime of the airfoil. Over the entire span of α, three-dimensional results consistently matched well with the two-dimensional predictions. It is concluded that stand alone two-dimensional simulations can determine the aerodynamic characteristics of airfoil with sufficient accuracy. Due to the limitation of space, only partial results at α=15° are presented in the present article.

4.5. Frequency spectrum of vortex shedding

Figure 5 depicts the oscillations in the aerodynamic coefficient for angle of attach greater than the stall angle ($\alpha = 13°$). Regular von-Karman vortex street is recognized with the instability in the values of flow variables inside the boundary layer for the two turbulence models. The vortex separation mechanism (roll up and detachment) from the surface affects the pressure distribution to cause intermittent fluctuation in the values of aerodynamic coefficients. The magnitude of these oscillations is similar for the two models. Spectral analysis was performed on the time series of the aerodynamic list coefficient to extract the dominant frequencies. Time history of the CFD

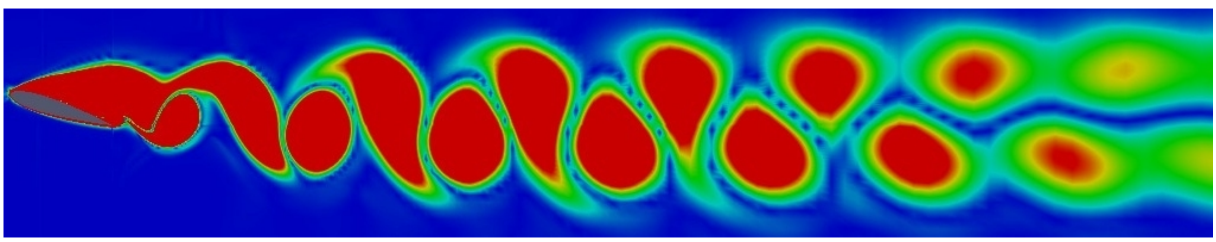

Figure 10: NACA0015: Vortex shedding in the wake region behind the airfoil. The alternating vortices induce unsymmetrical forces on the airfoil resulting in oscillatory behavior of the aerodynamic coefficients. The contours are plotted for $k-\omega$ SST at α=17°; Re=1.96x10^6.

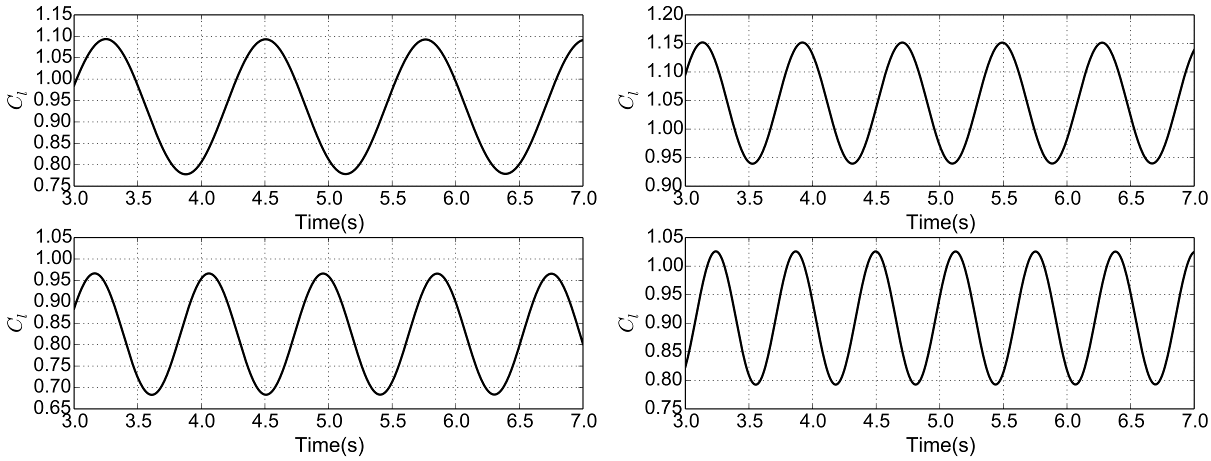

(a) $k-\epsilon$ (b) $k-\omega$ SST

Figure 11: NACA0015: Time evolution of drag and lift coefficients at α=15° (top) and α=17° (bottom) for two turbulence models. Higher vortex shedding is obtained for $k-\omega$ SST as compared to $k-\epsilon$ at a particular α.

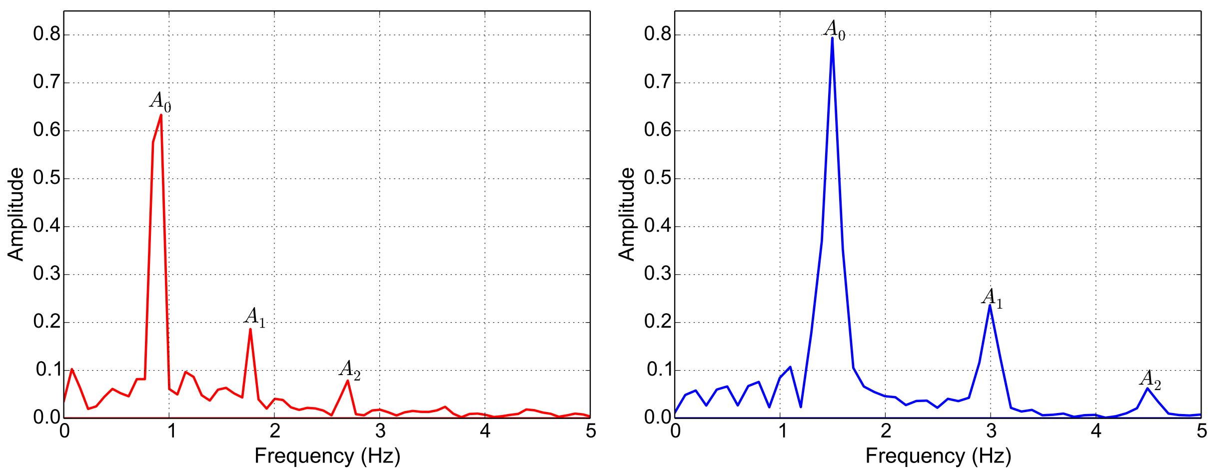

(a) $k-\epsilon$ (b) $k-\omega$ SST

Figure 12: NACA0015: Power spectra for the aerodynamic coefficients for lift at α=17° displaying the fundamental (f_s) and the even ($2f_s$) and odd ($3f_s$) harmonics together with its related amplitudes (A_0,A_1,A_2).

simulations constituted of approximately 10 seconds of the simulation length which corresponds to the periodic behavior over 20 complete cycles of vortex shedding. Figure 12 represents the power spectra of the lift fluctuations at $\alpha = 17°$ for $k{-}\omega$ SST and $k{-}\epsilon$ turbulence models. These fluctuations are comparable to the one obtained from the flows around circular cylinders [57]. A strong quadratic and cubic couplings is observed in the frequency harmonics (unlike to cylinder where only fundamental and odd coupling are observed [27]). The magnitude of the fundamental frequency at $\alpha = 17°$ is 0.9 and 1.5 for $k-\epsilon$ and $k-\omega$ SST models respectively. The second harmonic is exhibited at the quadratic frequency of 1.8 and 3.0 ($f_s + f_s = 2f_s$), whereas cubic coupling of the frequency is seen at $3f_s$. Both models have shown distinct magnitudes and peaks for the fundamental frequency and its quadratic and cubic couplings. The coupling of the rest of frequencies diminishes at higher α due to larger separation and less interaction with airfoil surface.

Model parameters				
	$k-\epsilon$		$k-\omega$ SST	
Parameter	$\alpha=15^\circ$	$\alpha=17^\circ$	$\alpha=15^\circ$	$\alpha=17^\circ$
x_0	0.48	0.62	0.55	0.8
x_1	0.11	0.188	0.17	0.25
x_2	0.02	0.07	0.03	0.06
$f_s(Hz)$	0.7	0.9	1.2	1.5
$\nu(rad/s)$	0.81	0.23	0.9	0.52
$\mathit{\Gamma}(rad/s)$	2.52	0.93	3.6	2.09
$\sigma(rad/s)$	1.63	0.96	2.81	2.22

Table 3: NACA0015: Model parameters required to solve the second order ODE for the proposed ROM equation to predict the aerodynamic coefficient C_l

4.6. The simplified, reduced order model

Based on the high fidelity solution and spectral decomposition of the time history of coefficients a ROM is developed to model lift. The proposed ROM is based on the van der Pol model [47]. The developed equation for the ROM is given by Equation 10

$$\ddot{C_l} + \varpi^2 C_l = \upsilon\dot{C_l} - \mathit{\Gamma} C_l\dot{C_l} - \varrho C_l^2\dot{C_l} \tag{10}$$

where, the parameters: $(\upsilon, \varrho, \varpi, \mathit{\Gamma})$ are all positive real numbers. Presence of term $C_l\dot{C_l}$ in the Equation 10 implies phase difference of around $\frac{\pi}{2}$ among the fundamental frequency and its first even harmonic. In Equation 10, the angular frequency ϖ is related to the actual shedding frequency $\varpi_s = 2\pi f_s$. Here, υ accounts for the linear damping, ϱ and $\mathit{\Gamma}$ represents the magnitudes of the nonlinear damping coefficients. The oscillator equation is solved employing the multiple scales method [24, 58]. The coefficients of the oscillator which are related to the damping are considered weak such that, $\upsilon = O(\kappa)$, $\varrho = O(\kappa)$ and $\mathit{\Gamma} = O(\kappa)$. The κ represents an artificial parameter using which we perform the expansion [59]. The proposed model thus becomes:

$$\ddot{C_l} + \varpi^2 C_l = \kappa(\upsilon\dot{C_l} - \mathit{\Gamma} C_l\dot{C_l} - \varrho C_l^2\dot{C_l}) \tag{11}$$

Seeking the relevant time-scales as $\delta_o = t, \delta_1 = \kappa t$ and $\delta_2 = \kappa^2 t$ and applying third-order expansion for Equation 11, we arrive at the following:

$$C_l(t) = C_{l_0}(\delta_0,\delta_1,\delta_2) + \kappa C_{l_1}(\delta_0,\delta_1,\delta_2) + \kappa^2 C_{l_2}(\delta_0,\delta_1,\delta_2) \tag{12}$$

The terms consisting of similar order of κ are equated to develop the following equation:

$$O(1) = \frac{\partial^2 C_{l_0}}{\partial\delta_o^2} + \varpi^2 C_{l_0} = 0 \tag{13}$$

$$O(\kappa) = \frac{\partial^2 C_{l_1}}{\partial\delta_o^2} + \varpi^2 C_{l_1} = -2\frac{\partial^2 C_{l_0}}{\partial\delta_o\partial\delta_1} + \upsilon\frac{\partial C_{l_0}}{\partial\delta_o} - \varrho C_{l_0}^2 \partial C_{l_0}\partial\delta_o - \mathit{\Gamma} C_{l_0}\frac{\partial C_{l_0}}{\partial\delta_o} \tag{14}$$

$$\begin{aligned} O(\kappa^2) = \frac{\partial^2 C_{l_2}}{\partial\delta_o^2} + \varpi^2 C_{l_2} = -2\frac{\partial^2 C_{l_1}}{\partial\delta_o\partial\delta_1} - \frac{\partial^2 C_{l_0}}{\partial\delta_1^2} + \upsilon\frac{\partial C_{l_1}}{\partial\delta_o} - \varrho C_{l_0}^2\frac{\partial C_{l_1}}{\partial\delta_o} + \upsilon\frac{\partial C_{l_0}}{\partial\delta_1} \\ -\varrho C_{l_0}^2\frac{\partial C_{l_0}}{\partial\delta_1} - 2\varrho C_{l_0}C_{l_1}\frac{\partial C_{l_0}}{\partial\delta_o} - \mathit{\Gamma} C_{l_0}\frac{\partial C_{l_1}}{\partial\delta_o} - \mathit{\Gamma} C_{l_0}\frac{\partial C_{l_0}}{\partial\delta_1} - \mathit{\Gamma} C_{l_1}\frac{\partial C_{l_0}}{\partial\delta_0} - 2\frac{\partial^2 C_{l_0}}{\partial\delta_o\partial\delta_2} \end{aligned} \tag{15}$$

Solution of Equation 13 is obtained as $C_{l_0} = A_0\cos(\varpi\delta_o + \beta_0)$. Thus the solution is incorporated in Equation 14 and expanded. After eliminating mixed secular terms, the solution becomes:

$$\dot{A_0} = \frac{4\upsilon A_0 - \varrho A_0^3}{8} \tag{16}$$

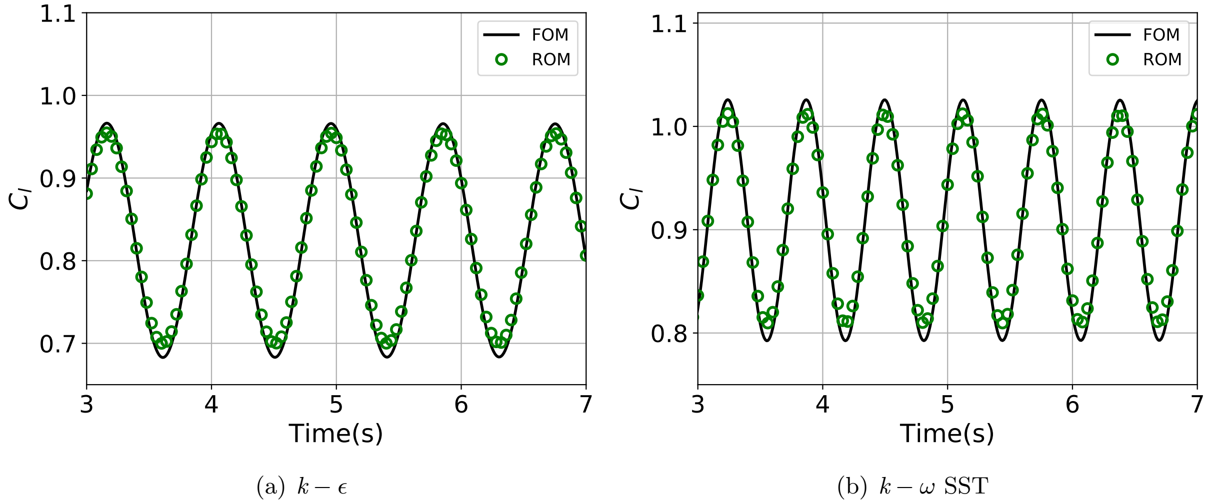

Figure 13: NACA0015: Comparison of the FOM (solid black line) and ROM (green circles) response in the time domain. The plot shows the comparison of aerodynamic lift coefficient. The ROM parameters are obtained by solving the second order ODE with the derived modal coefficients. The FOM solution is obtained by solving HF simulations considering all degrees of freedom

Applying the solutions for C_{l_0} and C_{l_1} in 15 and expanding all the terms, we get:

$$\dot{\beta}_0 = \frac{11\varrho^2 A_0^4 - 32\upsilon^2 + 48\upsilon\varrho A_0^2 + 32\Gamma^2 A_0^2}{256\varpi} \tag{17}$$

Equation 16-17 are called modulation equations. The following second-order approximate solution is thus obtained:

$$C_l = 2\sqrt{\frac{\upsilon}{\varrho}}\cos(\varpi\delta_o + \beta_0) - \frac{\Gamma A_0^2}{6\varpi}\cos(2\varpi\delta_0 + 2\beta_0 + \frac{\pi}{2}) - \frac{\varrho A_0^3}{32\varpi}\cos(3\varpi\delta_0 + 3\beta_0 + \frac{\pi}{2}) \tag{18}$$

The Equation 18 is simplified, and the amplitudes of; $\cos(\varpi\delta_o + \beta_0)$, $\cos(2\varpi\delta_0 + 2\beta_0 + \frac{\pi}{2})$, and $\cos(3\varpi\delta_0 + 3\beta_0 + \frac{\pi}{2})$ are denoted as A_0, A_1 and A_2, respectively. The amplitudes of these terms are obtained from the spectral decomposition of power spectra performed on transient Full Order Model (FOM) simulation data corresponding to each α and turbulence model. Calculating the steady-state solution from Equation 16 and performing integration over the terms in Equation 18, the model coefficients of A_0, A_1 and A_2 are computed as :

$$A_0 = 2\sqrt{\frac{\upsilon}{\varrho}}; \qquad A_1 = \frac{\Gamma A_0^2}{6\varpi}; \qquad A_2 = \frac{\varrho A_0^3}{32\varpi} \tag{19}$$

Solving the equations simultaneously with the damping model parameters becomes

$$\upsilon = \frac{8\varpi A_2}{A_0}; \qquad \varrho = \frac{32\varpi A_2}{A_0^3}; \qquad \Gamma = \frac{6\varpi A_1}{A_0^2} \tag{20}$$

The phase modulation term is given by

$$\begin{aligned} \varpi_s &= \varpi + \dot{\beta}_o \\ &= \varpi\left(1 - \frac{4A_2^2}{A_0^2} + \frac{9}{2}\frac{A_1^2}{A_0^2}\right) \end{aligned} \tag{21}$$

The model parameters $(\varpi, \upsilon, \varrho, \Gamma)$ are calculated using the magnitudes of first, second, and third harmonics computed from the spectral analysis (see Figure 12). After determining all the required parameters, Equation 10 is developed into an ODE and integrated using Runge-Kutta

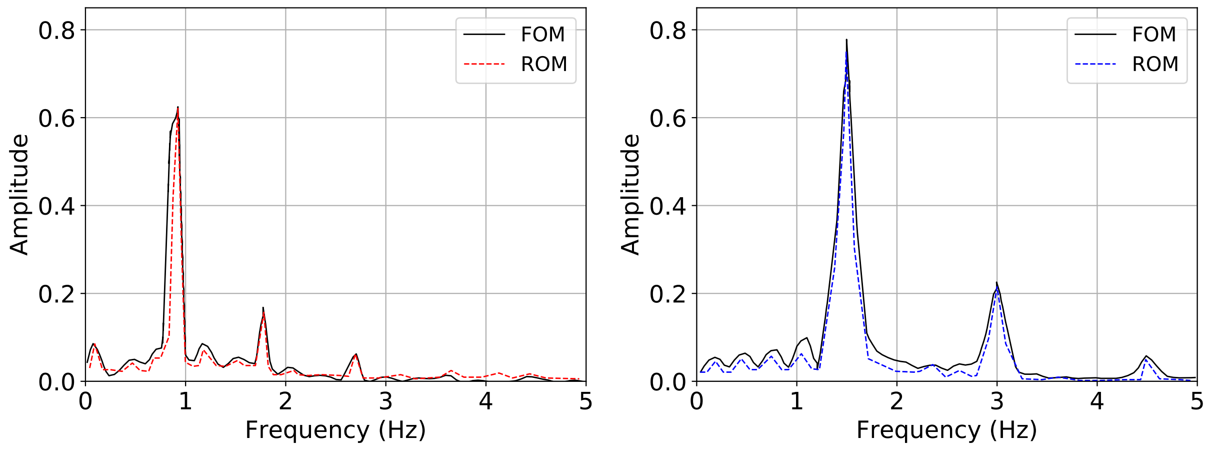

(a) $k - \epsilon$

(b) $k - \omega$ SST

Figure 14: NACA0015: Comparison of the FOM (solid black line) and ROM (dashed line) response in the spectral domain. The ROM spectral distribution is obtained by applying the Fast Fourier Transform to aerodynamic lift obtained in the time domain by solving the second-order ODE with the derived modal coefficients. The FOM spectral distribution is achieved by applying fast Fourier transform to aerodynamic lift obtained by solving HF simulations considering all degrees of freedom.

numerical routine. The obtained result of C_l from ROM is compared with FOM in Figure 13. The geometry parameter α is developed such that it can vary without altering the original ROM equation. The model parameters obtained for the k-ω SST and $k - \epsilon$ model at $\alpha = 15°,17°$ are summarized in the Table 3. Vortex shedding frequency increases with α and we obtain significantly higher magnitudes for $k - \omega$ SST model as compared to $k - \epsilon$. The ROM compares well with FOM regarding the overall trend of the time history of C_l. It can be seen that ROM slightly underestimates the extremal values; however, the overall quantification of error shows a deviation of less than 4%. In addition to the time domain, the main strength of the proposed ROM is its ability to capture well spectral domains. The strong first three harmonics are represented with reasonable accuracy for the k-ω SST and $k - \epsilon$ model at $\alpha = 15°,17°$ as shown in Figure 14. This manifests that aerodynamic characteristics can be accurately represented using proposed ROM in terms of aerodynamic lift coefficient with significantly less computational constraints. For instance, present FOM simulation takes approximately twenty minutes of simulation time to provide temporal lift coefficient running in parallel on four cores Intel Xeon E5-2680 v2. While ROM, corresponding to the reduced degree of freedom, predicted similar estimated values in less than two seconds, running in serial on a desktop computer with Intel i7-9700TE CPU.

4.7. ROM model in predictive settings

The proposed ROM model has shown remarkable improvements in terms of computational time and determining correct estimates of the aerodynamic loading of the lift coefficients, compared against the FOM. Herein the ROM capability is tested further in a predictive setting to access its validity for a wide range of operating conditions. C_l is computed at $\alpha = 16°$ using both high-fidelity simulation models and ROM approach. The model parameters are calculated through cubic interpolation from the data obtained for $\alpha = 15°,17°$ listed in Table 3. We obtained positive values of our damping parameters, which are reflective of the limit cycle. At the same time, magnitudes obtained at two different geometric parameters showed similar trends for the linear, quadratic, and cubic damping coefficients, which further highlights the accuracy of present ROM. We also notice a decreasing trend for damping parameter values at higher geometric incidence α, which is considered because of the drop in the C_l in the stall regime. The time histories for the C_l obtained by using FOM and ROM are displayed in Figure 15. It

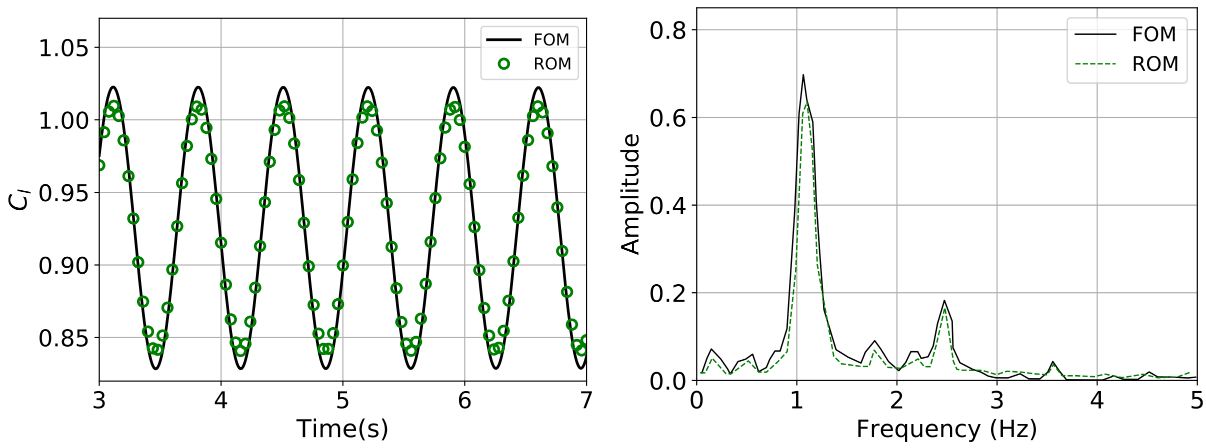

(a)

(b)

Figure 15: NACA0015: Comparison of the lift coefficient obtained with the FOM (HF simulations) and proposed ROM in a predictive setting (a) time-domain (b) spectral-domain at $\alpha = 16°$. The ROM spectral distribution is obtained by applying the Fast Fourier Transform to aerodynamic lift obtained in the time domain by solving the second-order ODE with the derived modal coefficients through cublic interpolation scheme. The FOM spectral distribution is achieved by applying fast Fourier transform to aerodynamic lift obtained by solving HF simulations considering all degrees of freedom.

can be observed that present ROM not only satisfies prediction in the time domain but also in the spectral domain. In order to effectively test quantification of error, percentage errors are compared from FOM and the ROM solution in terms of the fundamental frequency in the spectra. The reported error is found to be around 5%, which we consider acceptable given the significantly reduced computation time. Overall the proposed model performed extremely well in a predictive setting and able to capture very well the overall trend of the lifting behavior computed by the FOM.

5. Conclusions

Traditionally, oscillator models were proposed for determining the vortex induce vibrations around cylindrical structures. The current work presented the van der Pol based oscillator model for a study involving turbulent flow around the NACA0015 airfoil. The flow was simulated in two and three dimensions using three different RANS turbulence models (Spalart-Allmaras, $k-\epsilon$ and $k-\omega$ SST model). The numerical results were analyzed in both the time and frequency domains. The existence of both even and odd harmonics in the spectral analysis is reported for the airfoil (unlike the harmonics appearing in the cylindrical structures, which normally show odd couplings). Herein, a simplified ROM based on the van der Pol equation was proposed for the airfoil operation in the stall regime (with an additional term introduced to cater for the quadratic couplings), and its results were compared against the high fidelity simulations. Major findings of the work are enumerated below:

- Inside the attached ($0° \leq \alpha \leq 11°$) and mildly separated ($11° < \alpha \leq 13°$) regimes, all the three turbulence models illustrated a reasonable comparison, especially for the prediction of the aerodynamic lift. In the stall regime ($13° < \alpha \leq 17°$), $k-\omega$ SST and $k-\epsilon$ to certain extent, successfully captured the vortex shedding phenomena. SA model altogether failed to demonstrate the adverse pressure gradients around the airfoil. Insignificant differences between the 2D and 3D simulation results showed that the flow was not dominated by three-dimensional flow structures significant enough to affect the aerodynamic characteristics of the blade. Thus it can be concluded that in the absence of any tapering of the blade geometry along its length, 2D simulations suffices. When comparing the results across different turbulence models, $k-\omega$ SST turbulence model demonstrated superior performance.

- Strong quadratic and cubic non-linearities were identified in the temporal history of the lift coefficient. A ROM based on the van der Pol oscillator was proposed to model the aerodynamic lift coefficient at a higher angle of attacks. The model coefficients were computed using the results from high fidelity simulations. The addition of a quadratic nonlinearity to the ROM equation further improved its accuracy.
- The results obtained from the ROM compared well with the CFD result in the time domain. The model was then integrated to test the aerodynamic lift coefficient in a predictive setting, which correlated well with the high fidelity simulation results. The peaks were only observed to be 5% apart.

A turbine blade can be divided into an inner segment and an outer segment. While the former is designed with the structural integrity of the turbines in mind, the later is designed to maximize torque generation. It has been found in the past studies that flow around the outer sections of a blade remains attached to the surface. In such a situation, the ROM model proposed in this work can be useful. However, when it comes to the segment closer to the hub where massive flow separation takes place, the current ROM model will fail. For such a situation, we are in the process of developing a ROM model based on Proper Orthogonal Decomposition.

6. Acknowledgment

The authors acknowledge the financial support from the Norwegian Research Council and the industrial partners of *NOWITECH: Norwegian Research Centre for Offshore Wind Technology*, *OPWIND: Operational Control for Wind Power Plants* and *FSI-WT* (Grant No.:216465/E20) (http://www.fsi-wt.no). Furthermore, the authors greatly acknowledge the *Norwegian Metacenter for Computational science* (NOTUR-reference number: NN9322K/1589) for giving us access to the *Vilje* high-performance computer at the Norwegian University of Science and Technology (NTNU).

7. References

References

[1] Sarmast, S. *et al.* Validation of the actuator line and disc techniques using the new MEXICO measurements. *Journal of Physics: Conference Series* **753**, 032026 (2016).

[2] Zahle, F., Bak, C., Sørensen, N., Guntur, S. & Troldborg, N. *Comprehensive Aerodynamic Analysis of a 10MW Wind Turbine Rotor Using 3D CFD* (American Society of Mechanical Engineers, 2014).

[3] Bazilevs, Y. *et al.* 3D simulation of wind turbine rotors at full scale. part I: Geometry modeling and aerodynamics. *International Journal for Numerical Methods in Fluids* **65**, 207–235 (2011).

[4] Yang, H., Shen, W., Xu, H., Hong, Z. & Liu, C. Prediction of the wind turbine performance by using BEM with airfoil data extracted from CFD. *Renewable Energy* **70**, 107–115 (2014).

[5] Siddiqui, M. S., Rasheed, A., Kvamsdal, T. & Tabib, M. Effect of turbulence intensity on the performance of an offshore vertical axis wind turbine. *Energy Procedia* **80**, 312–320 (2015).

[6] Abbott, I. & Doenhoff, A. *Theory of wing sections. Including a summary of airfoil data* (Dover, New York, 1959).

[7] Morgado, J., Vizinho, R., Silvestre, M. & Pascoa, J. XFOIL vs CFD performance predictions for high lift low Reynolds number airfoils. *Aerospace Science and Technology* **52**, 207 – 214 (2016).

[8] Siddiqui, M. S., Durrani, N. & Akhtar, I. Quantification of the effects of geometric approximations on the performance of a vertical axis wind turbine. *Renewable Energy* **74**, 661–670 (2015).

[9] Siddiqui, M. S., Rasheed, A., Tabib, M. & Kvamsdal, T. Numerical investigation of modeling frameworks and geometric approximations on nrel 5MW wind turbine. *Renewable Energy* **132**, 1058 – 1075 (2019).

[10] Versteeg, H. K. & Malalasekerah, W. *An introduction to computational fluid dynamics: The finite volume method* (Harlow, Pearson Education Limited, 2007).

[11] Spentzos, A. *et al.* Investigation of three-dimensional dynamic stall using computational fluid dynamics. *Journal of American Institute of Aeronautics and Astronautics, AIAA* **43**, 1023–1033 (2005).

[12] Bai, Y., Sun, D., Lin, J., Kennedy, D. & Williams, F. Numerical aerodynamic simulations of a NACA airfoil using CFD with block-iterative coupling and turbulence modelling. *International Journal of Computational Fluid Dynamics* **26**, 119–132 (2012).

[13] Heggelund, Y., Skaar, I. & Jarvis, C. Interactive design of wind farm layout using CFD and model reduction of the steady state RANS equation. *11th World Wind Energy Conference, Bonn, Germany, 3-5 July* (2012).

[14] Heggelund, Y., Jarvis, C. & Khalil, M. A fast reduced order method for assessment of wind farm layouts. *Energy Procedia* **80**, 30 – 37 (2015).

[15] Solari, G., Carassale, L. & Tubino, F. Proper orthogonal decomposition in wind engineering - Part 1: A state-of-the-art and some prospects. *Wind and Structures* **10**, 153–176 (2007).

[16] Oliveira, I. B. & Patera, A. T. Reduced-basis techniques for rapid reliable optimization of systems described by affinely parametrized coercive elliptic partial differential equations. *Optimization and Engineering* **8**, 43–65 (2007).

[17] Parish, E. J. & Duraisamy, K. A paradigm for data-driven predictive modeling using field inversion and machine learning. *Journal of Computational Physics* **305**, 758 – 774 (2016).

[18] Tompson, J., Schlachter, K., Sprechmann, P. & Perlin, K. Accelerating eulerian fluid simulation with convolutional networks. *ArXiv e-prints* (2016). 1607.03597.

[19] Lee, C., Kim, J., Babcock, D. & Goodman, R. Application of neural networks to turbulence control for drag reduction. *Physics of Fluids* **9**, 1740–1747 (1997).

[20] Ling, J., Kurzawski, A. & Templeton, J. Reynolds averaged turbulence modelling using deep neural networks with embedded invariance. *Journal of Fluid Mechanics* **807**, 155–166 (2016).

[21] Ling, J. Using machine learning to understand and mitigate model form uncertainty in turbulence models. In *2015 IEEE 14th International Conference on Machine Learning and Applications (ICMLA)*, 813–818 (2015).

[22] Xiao, D. *et al.* Non intrusive reduced order modelling of the Navier-Stokes equations. *Computer Methods in Applied Mechanics and Engineering* **293**, 522 – 541 (2015).

[23] Bai, Z., Dewilde, P. M. & Freund, R. W. Reduced-order modeling. In *Handbook of numerical analysis. Vol XIII. Special volume: Numerical methods in electromagnetics.*, 825–895 (Amsterdam: Elsevier/North Holland, 2005).

[24] Nayfeh, A. H. *Introduction to perturbation techniques* (Wiley Classic Library Edition, 1993).

[25] Skop, R. A. & Balasubramanian, S. A new twist on an old model for vortex-induced vibrations. *Journal of Fluids and Structures* **11**, 395–412 (1997).

[26] Xu, K., Zhao, L. & Ge, Y. Reduced-order modeling and calculation of vortex-induced vibration for large-span bridges. *Journal of Wind Engineering and Industrial Aerodynamics* **167**, 228 – 241 (2017).

[27] Nayfeh, A. H., Owis, F. & Hajj, M. R. Model for the coupled lift and drag on a circular cylinder (DETC-2003 ASME 19th Biennial Conference on Mechanical Vibration and Noise, Orlando, Florida, USA, 2003).

[28] Qin, L. *Development of reduced-order models for lift and drag on oscillating cylinders with higher-order spectral moments.* PhD Thesis, Virginia Polytechnic Institute and State University, USA (2003).

[29] Akhtar, I. *Parallel simulation, reduced-order modeling and feedback control of vortex-shedding using fluidic actuators.* PhD Thesis, Virginia Polytechnic Institute and State University, USA (2008).

[30] Stabile, G., Matthies, H. G. & Borri, C. A novel reduced order model for vortex induced vibrations of long flexible cylinders. *Ocean Engineering* **156**, 191 – 207 (2018).

[31] Ghias, R., Mittal, R. & Dong, H. Study of tip vortex formation using large eddy simulation. *43th Fluid Dynamics Conference and Exhibit, Renp, Nevada* **35**, AIAA–2005–1280 (10-13 January, 2005).

[32] Cottrell, J. A., Hughes, T. J. R. & Bazilevs, Y. *Isogeometric Analysis: Toward Integration of CAD and FEA* (1st edn. Wiley Publishing, 2009).

[33] Nordanger, K., Holdahl, R., Kvarving, A. M., Rasheed, A. & Kvamsdal, T. Implementation and comparison of three isogeometric Navier-Stokes solvers applied to simulation of flow past a fixed 2D NACA0012 airfoil at high Reynolds number. *Computer Methods in Applied Mechanics and Engineering* **284**, 664–688 (2015).

[34] Nordanger, K., Holdahl, R., Kvamsdal, T., Kvarving, A. M. & Rasheed, A. Simulation of airflow past a 2D NACA0015 airfoil using an isogeometric incompressible Navier-Stokes solver with the Spalart-Allmaras turbulence model. *Computer Methods in Applied Mechanics and Engineering* **290**, 183 – 208 (2015).

[35] Tang, D. M. & Dowell, E. H. Experimental investigation of three-dimensional dynamic stall model oscillating in pitch. *Journal of Aircraft* **32**, 1062–1071 (1995).

[36] Shur, M. L., Spalart, P. R., Strelets, M. K. & Travin, A. K. A hybrid RANS-LES approach with delayed-DES and wall-modelled LES capabilities. *International Journal of Heat and Fluid Flow* **29**, 1638 – 1649 (2008).

[37] Piziali, R. An experimental investigation of 2D and 3D oscillating wing aerodynamics for a range of angle of attack including stall. *NASA Technical Memorandum 4632* (1993).

[38] Wernert, P., Geissler, W., Raffel, M. & Kompenhans, J. Experimental and numerical investigations of dynamic stall on a pitching aerofoil. *AIAA Journal* **35**, 982–989 (1996).

[39] Schreck, S. J. & Hellin, H. E. Unsteady vortex dynamics and surface pressure topologies on a finite pitching wing. *Journal of Aircraft* **31**, 899–907 (1994).

[40] Durbin, P. *A perspective on recent developments in RANS modeling* (Elsevier Science Ltd, Oxford, 2002).

[41] Miller, A., Chang, B., Issa, R. & Chen, G. Review of computer-aided numerical simulation in wind energy. *Renewable and Sustainable Energy Reviews* **25**, 122–134 (2013).

[42] Spalart, P. & Allmaras, S. A one-equation turbulence model for aerodynamic flows. *AIAA Paper 92-0439(1992)* .

[43] Wilcox, D. Simulation of transition with a two-equation turbulence model. *AIAA Journal. 32* 247–255 (1994).

[44] Kato, M. & Launder, B. E. The modelling of turbulent flow around stationary and vibrating square cylinders. August 16–18 (Ninth Symposium on Turbulent Shear Flows, Japan, 1993).

[45] Menter, F. Two-equation eddy-viscosity turbulence models for engineering applications. *AIAA Journal. 32* 1598–1605 (1994).

[46] Singh, R. K., Ahmed, M. R., Zullah, M. A. & Lee, Y. H. Design of a low Reynolds number airfoil for small horizontal axis wind turbines. *Renewable Energy* **42**, 66–76 (2012).

[47] Nayfeh, A. H., Owis, F. & Hajj, M. R. A model for the coupled lift and drag on a circular cylinder. In *Proceedings of DETC2003, ASME 19th Biennial Conference on Mechanical Vibration and Noise* (ASME, 2003). DETC2003/VIB-48455.

[48] Liu, F. *Thorough description of how wall functions are implemented in OpenFOAM* (In Proceedings of CFD with OpenSource Software, 2016).

[49] Jasak, H. Error analysis and estimation in the finite volume method with applications to fluid flows. *Imperial College, University of London* (1996).

[50] Jasak, H. Dynamic mesh handling in OpenFOAM. *47th AIAA Aerospace Sciences Meeting Including the New Horizons Forum and Aerospace Exposition* **52**, (AIAA 2009–341) (5-8 January, 2008).

[51] Broeckhoven, T., Smirnov, S., Ramboer, J. & Lacor, C. Finite volume formulation of compact upwind and central schemes with artificial selective damping. *Journal of Scientific Computing* **21**, 341–367 (2004).

[52] Liao, Q., Dong, G. J. & Lu, X. Y. Vortex formation and force characterisitics of a foil in the wake of a circular cylinder. *Journal of Fluids and Structures* **19**, 491–510 (2004).

[53] Tabib, M., Rasheed, A., Siddiqui, M. S. & Kvamsdal, T. A full-scale 3D vs 2.5D vs 2D analysis of flow pattern and forces for an industrial-scale 5MW NREL reference wind-turbine. *Energy Procedia* **137**, 477 – 486 (2017).

[54] Tachos, N. S., Filios, A. E. & Margaris, D. P. A comparative numerical study of four turbulence models for the prediction of horizontal axis wind turbine flow. *Proceedings of the Institution of Mechanical Engineers, Part C: Journal of Mechanical Engineering Science* **224**, 1973–1979 (2010).

[55] Wilcox, D. *Turbulence Modeling for CFD* (DCW Industries Inc. La Canada CA, 1993).

[56] Sagmo, K. F., Bartl, J. & Sætran, L. Numerical simulations of the NREL S826 airfoil. *Journal of Physics: Conference Series* **753**, 082036 (2016).

[57] Nayfeh, A. H., Marzouk, O. A., Arafat, N. H. & Akhtar, I. Modeling the transient and steady-state flow over a stationary cylinder. In *Proceedings of DETC-2005 ASME Design Engineering Technical Conference* (2005).

[58] Nayfeh, A. H. *Perturbation methods* (Wiley Classic Library Edition, 2000).

[59] Kevorkian, J. & Cole, J. D. *Multiple scale and singular perturbation methods* (Springer, 1996).